Excitonic Energy Migration in Conjugated Polymers: The Critical Role of Interchain Morphology

ARTICLE *in* JOURNAL OF THE AMERICAN CHEMICAL SOCIETY · SEPTEMBER 2014

Impact Factor: 12.11 · DOI: 10.1021/ja508112k · Source: PubMed

JACS
JOURNAL OF THE AMERICAN CHEMICAL SOCIETY
Article
pubs.acs.org/JACS

Excitonic Energy Migration in Conjugated Polymers: The Critical Role of Interchain Morphology

Zhongjian Hu,[†] Takuji Adachi,[†] Ryan Haws,[†] Bo Shuang,[‡] Robert J. Ono,[†] Christopher W. Bielawski,[†] Christy F. Landes,[‡] Peter J. Rossky,[†] and David A. Vanden Bout*[,†]

[†]Center for Nano and Molecular Science and Technology, Department of Chemistry, University of Texas, Austin, Texas 78712, United States

[‡]Department of Chemistry, Rice University, Houston, Texas 77251, United States

Supporting Information

ABSTRACT: Excitonic energy migration was studied using single molecule spectroscopy of individual conjugated polymer (CP) chains and aggregates. To probe the effect of interchain morphology on energy migration in CP, tailored interchain morphologies were achieved using solvent vapor annealing to construct polymer aggregates, which were then studied with single aggregate spectroscopy. We report that highly ordered interchain packing in *regioregular* poly(3-hexylthiophene) (*rr*-P3HT) enables long-range interchain energy migration, while disordered packing in *regiorandom* poly(3-hexylthiophene) (*rra*-P3HT), even in aggregates of just a few chains, can dramatically impede the interchain mechanism. In contrast to *rr*-P3HT, interchain energy migration in poly(3-(2′-methoxy-5′-octylphenyl)thiophene) (POMeOPT), a polythiophene derivative with bulky side chains, can be completely inhibited. We use simulated structures to show that the reduction in interchain coupling is not due simply to increased packing distance between backbones of different chains, but reflects inhibition of stacking due to side-chain-induced twisting of the contours of individual chains. A competition from intrachain coupling has also been demonstrated by comparing POMeOPT aggregates with different polymer chain sizes.

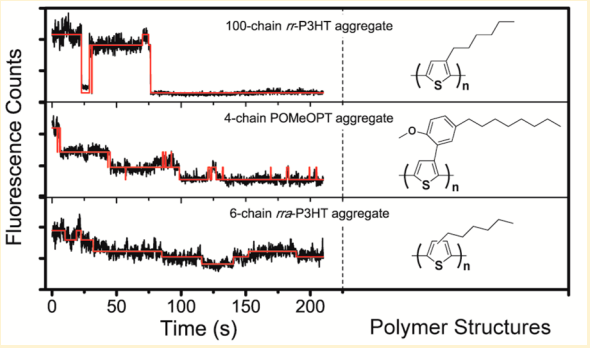

INTRODUCTION

Conjugated polymers (CPs) have been of wide interest as organic semiconductors in various optoelectronic applications due to the advantageous and unique combination of excellent optoelectronic properties, synthetic versatility, and mechanical flexibility.[1] Upon photoexcitation the primary excitation in CPs is typically a Coulombically bound exciton (electron−hole pair). The initially created exciton can be delocalized both along and between polymer chains.[2] The energy landscape for these excitons is governed by intra- and interchain conformations as well as dynamics. Following excitation, the exciton relaxes and localizes in the low energy minima. On longer time scales, excitonic energy migration proceeds via a hopping mechanism along and between polymer chains.[2b,3] The development of CPs for optoelectronic applications requires a detailed and essential understanding of these dynamics due to their key role in determining the material functions and ultimate device performance.[2b,4] For instance, with respect to polymer solar cells, long-range excitonic energy migration is desired for efficient exciton dissociation and charge generation at the interface between CPs and electron accepting materials. In contrast, for light emitting diodes, a short migration distance is favorable to avoid exciton quenching at defects.

Due to the unique structures of CPs, the aforementioned excitonic dynamic processes can occur along a polymer chain (intrachain) and across stacked polymer chains (interchain).[2b,5] Consequently, the conformation of single polymer chains and the manner in which they pack collectively influence the exciton dynamics in CP films. The interchain energy migration is of more relevance to practical applications which usually involve bulk films where the polymer chains are closely packed. The interchain energy migration is a strong function of interchain structures including packing order and distance. In most cases, this structure−property relationship is difficult to unravel via measurements on bulk samples due to the structural complexity of thin films. For example, consider the prototypical polythiophenes. It has been argued that, in *rr*-P3HT bulk films, there exists two-dimensional (i.e., interchain and intrachain) exciton migration, while, in *rra*-P3HT films, the exciton is strongly intrachain localized.[6] However, it remains unclear if this difference is caused by disordered single chain conformations or disordered packing among the polymer chains, or both. In addition to the interchain structural ordering, interchain packing distance is another important factor that affects the energy migration between polymer

Received: August 7, 2014
Published: September 30, 2014

dx.doi.org/10.1021/ja508112k | J. Am. Chem. Soc. 2014, 136, 16023−16031

chains. Long (short) interchain packing distance reduces (increases) the electronic coupling between polymer chains, therefore weakening (promoting) interchain energy migration. Moreover, the scheme of energy migration in CPs can be complicated by the heterogeneity of couplings along and between polymer chains. Recent investigations on *rr*-P3HT nanostructures have indicated that there is a delicate interplay between the intrachain and the interchain electronic couplings.[7] These studies demonstrate that short-range intrachain order and strong interchain interaction lead to dominant interchain coupling (resembling H-aggregate behavior). In contrast, long-range intrachain order and weak interchain interaction result in strong intrachain coupling (resembling J-aggregate behavior).

Despite extensive studies on the influence of morphology on energy migration in CPs, in-depth insight into the *interchain* and *intrachain* morphological dependence of energy migration is strongly obscured by ensemble-averaged measurement on bulk states that usually involve high morphological heterogeneity due to various single chain conformations and chain aggregations.[8] To disentangle the intrachain and the interchain energy migration mechanisms and to probe their dependence on morphology, it is necessary to combine a material system with tailored structural characteristics and a characterization technique that goes beyond the ensemble average. Single molecule/aggregate spectroscopy has proven to be an unprecedented and powerful method for providing a molecular understanding of the relationships between polymer morphologies and photophysical properties.[8,9] For instance, the morphological order of single polymer molecules/aggregates can be monitored via single molecule/aggregate fluorescence excitation polarization.[10] In this experiment, the fluorescence intensity trace is modulated with a rotating linearly polarized excitation light and then fitted with $I(\alpha) \propto 1 + M \cos 2(\alpha - \phi)$, where α is the excitation polarization angle and ϕ is the polarization angle at maximum absorption. The modulation depth, M, represents the anisotropy of the absorption (excitation) tensor projected on the $x-y$ plane of the laboratory frame and is related to the morphological order of individual molecules or aggregates.[10] At the same time, the efficient energy migration in single molecules/aggregates can be manifested by fluorescence blinking statistics resulting from randomly generated photochemical quenchers, such as radical cations.[11] The blinking reflects the accessibility of the quenching site from any location of initial excitons. Therefore, large quenching is interpreted as resulting from rapid exciton migration to the quenching site. Thus, large intensity jumps are diagnostic of extensive excitonic energy migration.[11]

The influence of single chain morphology on excitonic energy migration can be examined by comparing the photophysics of single molecules of *rr*- and *rra*-P3HT (Scheme 1) in the presence of photochemical quenchers randomly generated at high laser excitation power density (~90 W/cm^2).[11] Herein, *rr*- and *rra*-P3HT have the same number average molecular weight, M_n, of 146 kDa and dispersity, Đ, of 1.20. The *rr*-P3HT single molecules exhibit a pronounced fluorescence blinking, suggesting an efficient energy migration in these highly ordered single chains (see Figures S1A and S1C in the Supporting Information). This observation of pronounced blinking in *rr*-P3HT is consistent with our previous report based on photoluminescence spectra and theoretical modeling.[12] Despite a disordered single chain conformation (Figure S1D in the Supporting Information),[12,13] single *rra*-P3HT molecules also exhibit fluorescence intermittency (Figure S1B in the Supporting Information), indicative of efficient energy migration. This is probably caused by the formation of low energy trap sites due to the folding of single *rra*-P3HT chain. In addition, the intrachain energy migration to such low energy sites along the polymer chain in *rra*-P3HT might be more effective than in *rr*-P3HT due to a more heterogeneous distribution of chromorphore conjugation length in the former.[14] Nevertheless, the comparison of *rr*- and *rra*-P3HT single molecules reveals limited information regarding the precise relationship between the morphology and the intrachain and interchain excitonic energy migration. As such, the design of specific polymer structures that can disentangle interchain from intrachain morphological effects is warranted.

Herein, single polymer chains were assembled into aggregates with tailored interchain morphologies using a solvent vapor annealing (SVA) technique.[11b] The polymers used for aggregate preparation were of low molecular weight, thus largely eliminating intramolecular backbone contact interactions due to folding. The control of the interchain packing morphology in these aggregates, i.e., packing ordering and distance, was realized through varying regioregularity and size of side chains, respectively. Specifically, the tuning of the interchain packing order was realized by employing *rr*- and *rra*-P3HT, while one anticipates altering of the interchain packing distance via a bulky side-chain polythiophene derivative, poly(3-(2′-methoxy-5′-octylphenyl)thiophene) (POMeOPT, Scheme 1), in comparison to the *rr*-P3HT. As described below, single aggregate spectroscopy of the tailored aggregate structures was used to delineate how the aforementioned expectations were expressed in terms of influencing the excitonic energy migration. In addition, by comparing POMeOPT aggregates composed of different polymer chain size, the competition between interchain and intrachain energy migration mechanisms was examined.

Scheme 1. Chemical Structures of *rr*-P3HT, *rra*-P3HT, and POMeOPT

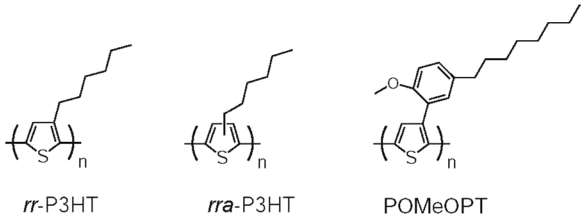

EXPERIMENTAL SECTION

Materials. *rr*-P3HT (97% head-to-tail (HT) coupling), *rra*-P3HT (64% HT), and POMeOPT (85% HT) were synthesized using literature reported methods.[13a,15] The polymers were further fractionated with gel permeation chromatography (GPC, GPCmax VE-2001, Viscotek) to get desired molecular weight (M_n) with a dispersity (Đ) below 1.2. For the fabrication of polymer aggregates, to avoid possible interchain packing arising from the folding of single chains, P3HT with M_n of 10 kDa was used.[16] The M_n of POMeOPT was chosen to be 19 kDa unless specified to ensure that the number of thiophene repeating units (~60) is similar to that of 10 kDa P3HT. Poly(methyl methacrylate) (PMMA, M_n = 45 kDa, Đ = 2.2) was purchased from Sigma-Aldrich. Dry solvents including toluene, chloroform, and acetone were purchased from Acros Organics. Glass coverslips were cleaned in an acid piranha solution (1:3 v/v hydrogen peroxide and sulfuric acid) and thoroughly rinsed with nanopure water before use.

dx.doi.org/10.1021/ja508112k | J. Am. Chem. Soc. 2014, 136, 16023−16031

Aggregate Preparation. For P3HT, both the single molecule samples and the concentrated precursor samples for the preparation of aggregates using the SVA method were spin-cast in a N_2 filled glovebox from toluene solutions containing 6 wt % PMMA on clean coverslips. This process afforded a 200 nm thick PMMA film with conjugated polymer chains embedded inside. The number of chains (~4000 for *rr*-P3HT and ~500 for *rra*-P3HT in the field of view) in the precursor concentrated films was estimated using the dilution factor based on the number of chains observed in diluted single molecule samples. Since POMeOPT has a poor solubility in toluene,[17] the POMeOPT single molecule sample and the precursor concentrated samples for SVA were spin coated from chloroform solutions containing 2 wt % PMMA on clean coverslips to yield 200 nm thick films. The precursor concentrated samples for SVA had ~400 POMeOPT chains. The polythiophene aggregates were obtained using the SVA technique reported previously.[11b] During SVA, the host matrix PMMA was exposed to N_2 gas saturated with solvent vapor by purging N_2 through a reservoir of the solvent mixture of chloroform and acetone. Chloroform is a good solvent for both PMMA and polythiophene, whereas acetone is a bad solvent for polythiophene that results in polythiophene aggregation but still capable of swelling PMMA. A solvent mixture of chloroform (good) and acetone (bad) at a vapor ratio of V_g/V_b = 22/78 (volume ratio of 40/60) was used unless otherwise specified. The diffusion of the polythiophene single chains inside the swollen liquid- and/or solid-like PMMA matrix results in the generation of polythiophene aggregates. The SVA experiment was typically carried out for 40 min. After SVA, the solvent vapor was stopped, and then the samples were purged to dryness using pure N_2 gas for 10 min. The number of chains in polymer aggregates (i.e., the size of aggregates) was then estimated based on the change in the number of emitting spots before and after SVA. An intensity threshold above the intensity of single chains was applied to the SVA treated samples to measure primarily the number of aggregates. A detailed description of the method with an example is provided in the Supporting Information.

Single Molecule/Aggregate Spectroscopy. The measurements for the single molecules and the aggregates were all conducted under N_2 atmosphere. The wide-field optical microscopy is based on an inverted microscope (Zeiss, Axiovert 200) with a 1.25 NA objective lens (Zeiss, Achrostigmat, 100× , oil immersion) and has been described in detail previously.[10b] Briefly, a collimated Ar ion laser beam at 488 nm (Melles Griot, model 35 LAL-030-208) with a power density of ~1.5 W/cm^2 was used to excite the molecules in an area with a diameter of ~40 μm at fwhm. For the fluorescence excitation polarization experiment, a rotating linearly polarized excitation light was obtained via a combination of an electro-optical modulator (Fastpulse technology, model 3079-4) and a quarter-wave plate. The fluorescence signal was filtered with a dichroic mirror and 488 nm notch filter (Chroma) and then detected with an EMCCD detector (Andor, model iXon+ DU-897E) under wide-field detection scheme. The fluorescence transients and spectra were taken under sample-scanning confocal mode using the same microscope and objective lens as in the wide-field microscopy mode. The emission spectra were taken at an excitation power of ~30 W/cm^2. The emitted light was filtered with a 496 nm blocking edge long-pass filter (Semrock) and delivered to a spectrograph (Princeton Instruments Acton SP-150) that was coupled to a liquid N_2 cooled CCD camera (Princeton Instruments). The spectrum of single molecule or aggregate was obtained by averaging over 4 consecutive spectra collected with an integration time of 10 s each. Transient fluorescence was collected with an avalanche photodiode detector (PerkinElmer, SPCM-AQR-16) with an exposure time of 100 ms under N_2, with a high laser power density (~90 W/cm^2) to induce blinking behavior due to generation of photochemical quenchers. It should be noted that fluorescence blinking events (i.e., photogenerated quenchers) were initiated under high laser power excitation. Under the normal excitation power used for imaging, most aggregates were stable without showing any blinking.

RESULTS AND DISCUSSION

Effect of Interchain Packing Ordering on Energy Migration. Figure 1 shows wide-field fluorescence images of *rr*-P3HT in PMMA before (A) and after SVA (B). Based on the variation of the numbers of fluorescent spots before and after SVA, the aggregates are estimated to be composed of ~100 ± 15 *rr*-P3HT single chains (hereafter denoted as 100-chain *rr*-P3HT aggregates for simplicity). Despite the large number of component chains, the 100-chain *rr*-P3HT aggregates have fluorescence intensity only ~3 times higher than single chains.

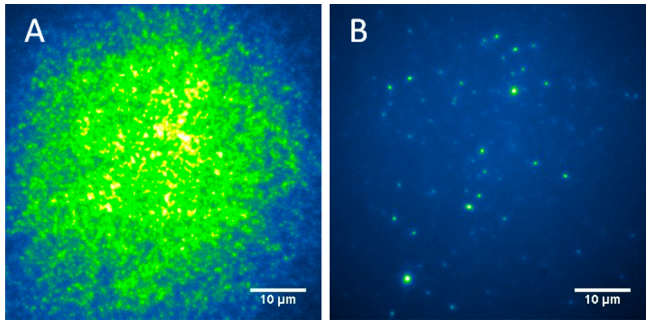

Figure 1. Wide-field fluorescence images of *rr*-P3HT (A) before and (B) after SVA; *rr*-P3HT aggregates composed of ~100 chains were formed after SVA.

This substantial fluorescence quenching has been attributed to nonradiative decay channels induced by strong interchain interaction possibly involving charge-transfer character in the excited state,[18] the formation of nonemissive H-aggregates,[19] the singlet exciton quenching by the triplet,[9a] and the generation of polaron pairs from hot excitons.[6b] In contrast to *rr*-P3HT, the aggregates of *rra*-P3HT are much smaller, i.e., ~6 ± 1 chains (hereafter denoted as 6-chain *rra*-P3HT aggregate for simplicity), under the same SVA conditions. The much smaller size of the *rra*-P3HT aggregates is likely due to unfavorable stacking interaction between *rra*-P3HT chains[20] and/or the higher solubility of *rra*-P3HT relative to *rr*-P3HT in both acetone and chloroform which could result in smaller aggregates in the SVA process.[11b,21] Another pronounced difference between the *rr*-P3HT and *rra*-P3HT aggregates lies in their fluorescence intensity. In contrast to the large drop in fluorescence quantum yield seen for *rr*-P3HT aggregates, the intensity of *rra*-P3HT aggregates was approximately proportional to the number of constituent chains. This implies that the nonradiative channels proposed for the case of the *rr*-P3HT aggregates are absent in the *rra*-P3HT aggregates. More importantly, it provides clear evidence that the aforementioed nonradiative channels are strongly associated with the interchain interaction due to a high degree of packing order and the resultant efficient energy migration.

To examine the morphological order, i.e., the degree of alignment of chromophores, the fluorescence intensity modulation depth, *M*, from individual aggregates was extracted by using fluorescence excitation polarization spectroscopy.[22] Herein, *M* measures the degree of alignment of chromophores in any single aggregate. As shown in Figure 2A, the *rr*-P3HT aggregates exhibit a high mean *M* value peaked at 0.80 with only a small probability of *M* below 0.60, reflecting a high interchain packing order in the aggregates. The aggregates have higher *M* values with a narrower distribution compared to the single *rr*-P3HT chains (Figure S3A in the Supporting

dx.doi.org/10.1021/ja508112k | J. Am. Chem. Soc. 2014, 136, 16023−16031

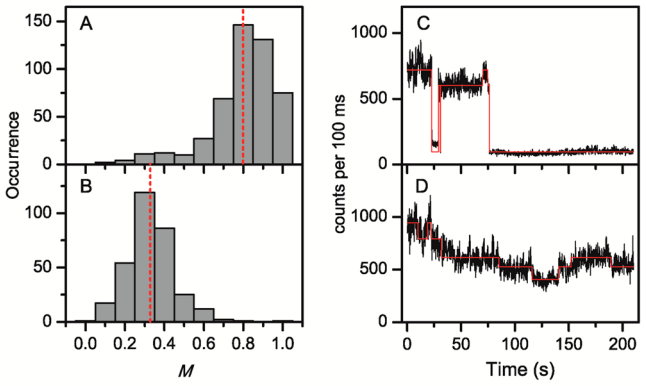

Figure 2. Histograms of fluorescence intensity modulation depth, *M*, of (A) 100-chain *rr*-P3HT aggregates and (B) 6-chain *rra*-P3HT aggregates. The red dashed lines represent the mean *M*. Typical fluorescence transients are displayed in panels C and D corresponding to the *rr*- and *rra*-P3HT aggregates, respectively, with the denoised data overlaid in red. Note that the background signal in the transients is ∼20 counts/100 ms. More fluorescence transients for *rr*- and *rra*-P3HT aggregates can be found in Figure S4 in the Supporting Information.

Information), indicating that the interchain stacking improves the conformational order of individual component chains. In stark contrast to *rr*-P3HT, *rra*-P3HT aggregates comprising only 6 chains exhibit an average *M* value of 0.33 with the large majority of *M* values below 0.50, as shown in Figure 2B. Given that the 10 kDa *rra*-P3HT single chains exhibit only slightly lower mean *M* value and broader *M* distribution (Figure S3B in the Supporting Information) with respect to the 10 kDa *rr*-P3HT chains, the low *M* values of the *rra*-P3HT aggregates demonstrate morphological disorder in interchain packing. The substantial difference in the interchain packing morphology between the *rr*-P3HT and the *rra*-P3HT aggregates unambiguously underscores the critical role which regioregularity plays in directing the interchain morphology.

The role of interchain morphology on interchain energy migration was next explored by examining the fluorescence blinking behavior of individual aggregates in the presence of random generation of photochemical quenchers at high laser excitation power density. The energy migration length scale in the aggregates can be accessed from the distribution of fluorescence quenching depth (QD), extracted from blinking events of each aggregate using our previously reported method.[11b] Briefly, the maximum intensity was obtained first by averaging the ten highest data points within the transients; then a quenching or dequenching step was determined using a threshold based on the noise level (see Experimental Section and ref 11b for details). Due to the low fluorescence efficiency of polythiophene aggregates and other forms of noise in the fluorescence trajectories, the accurate QD values however are not easily obtained using the raw data directly. To provide a more quantitative analysis, we applied a recently developed denoising method to the fluorescence trajectories to objectively resolve the underlying intensity levels (i.e., the number of emissive states),[23] a brief description of which follows. First, a Student's *t* test was iteratively used to detect all the intensity transitions that break the fluorescence trajectory into segments. Then, the segments were grouped into an optimal number of states, determined on the basis of the minimum description length principle (see the Supporting Information for details). As depicted in Figures 2C and 2D, the denoised trajectories overlaid the raw data and exhibited distinct intensity levels which effectively provided an accurate determination of the true number of discrete emitters as well as of the quenching depth value for each transition. These denoised trajectories were then used in further QD analysis. As presented in Figure 2C, discrete fluorescence blinking has been observed for the 100-chain *rr*-P3HT aggregates, indicative of efficient interchain energy migration within these aggregates. With respect to the 100-chain *rr*-P3HT aggregates, the mean value of QD was observed to be ∼46% and QD values even larger than 70% have been observed for ∼22% of the aggregates (Figure S6A in the Supporting Information). Larger 330 ± 30 chain *rr*-P3HT aggregates (hereafter denoted as 330-chain *rr*-P3HT aggregates for simplicity) can be assembled by using a relatively slow vapor rate during SVA. This is likely due to the fact that the slower vapor rate effectively increases the fraction of choloform in the film and an increase of good solvent proportion tends to result in larger aggregate size.[11b] For these large 330-chain *rr*-P3HT aggregates, the QD mean value decreases to 31% with a small population above 70% (Figure S6B in the Supporting Information). The reduced size of the QD is attributed to the formation of morphologically distinct and unaligned polymer domains, as indicated by the distribution of lower *M* values (Figure S6D in the Supporting Information). Hence, rapid energy migration only occurs within domains in the larger aggregates. At present, the exact dimensions of aggregates are unknown due to challenges in characterizing aggregates immersed in the PMMA matrix. Previous studies showed that the size of the nucleus in *rr*-P3HT crystallization is dependent on the degree of supercooling ΔT_c, which is the difference between the melting temperature T_m and the crystallization temperature T_c.[24] The temperature dependence of the nucleus size is believed to be responsible for the similarity in the observed cross-section size (i.e., thickness and width of nanofibers) of P3HT nanostructures reported in the literature.[24,25] Based on previous results, the dimensions of the 100- and 330-chain *rr*-P3HT aggregates in the present work can be estimated (Figure S7 in the Supporting Information). With the QD values and these proposed dimensions, the mean interchain energy migration length is estimated to be ∼5−15 nm. However, ultralong-range energy migration, up to ∼30−40 nm, was indicated for some cases in the large 330-chain *rr*-P3HT aggregates (see Figure S7 and corresponding discussions in the Supporting Information).

Despite being composed of only ∼6 chains, the *rra*-P3HT aggregates exhibit a rather slow and quite gradual fluorescence decay in Figure 2D. The absence of pronounced *discrete* blinking behavior in such small *rra*-P3HT aggregates signifies that the interchain energy migration is dramatically restricted in these disordered aggregates. The slow and gradual photobleaching also implies that the intrachain electronic coupling is not delocalized; otherwise a stepwise (chain-by-chain) fluorescence fluctuation would be expected in aggregates with only a few *rra*-P3HT chains. On the basis of the distinction in fluorescence transients and the number of component chains in the *rr*-P3HT and the *rra*-P3HT aggregates, it can be roughly estimated that the efficiency of interchain energy migration in the disordered *rra*-P3HT aggregates is at least several decades less, if there is any, than in the ordered *rr*-P3HT aggregates. The above comparison clearly points out that the interchain morphology plays an extremly significant role in affecting the energy migration process in CPs. Therefore, means that can

dx.doi.org/10.1021/ja508112k | J. Am. Chem. Soc. 2014, 136, 16023−16031

improve the interchain morphology such as increasing the side-chain regioregularity and optimizing the packing order via post-treatment are of great consequence for long-range energy migration.

Impact of Interchain Packing Distance on Energy Migration. In the cases considered so far in this work, it appears that the control of interchain energy migration via tuning the extent of interchain ordering ends up with two extremes. That is, in the highly ordered *rr*-P3HT aggregates, interchain morphology leads to very efficient interchain energy migration, while, in the disordered *rra*-P3HT aggregates, interchain energy migration is almost completely shut off even between a small number of chains. In addition to the interchain alignment, the interchain packing distance is another important factor that controls energy migration between polymer chains. Therefore, the next question is: to what extent can interchain energy migration be affected by the interchain packing distance? To attempt to address this question, we synthesized POMeOPT (Scheme 1), a polythiophene derivative with a bulky octylphenyl side chain, and investigated its excitonic energy migation in comparison to P3HT. Compared to the pi−pi stacking distance of ∼3.8 Å expected in *rr*-P3HT, an estimated interchain pi−pi stacking distance of ∼7 Å was previously reported for POMeOPT.[17] First, we examined the single chain conformation of POMeOPT with fluorescence excitation anisotropy. The single POMeOPT (19 kDa) chains exhibit a mean M value of 0.62 (Figure S8A in the Supporting Information), slightly lower than that of 10 kDa *rr*-P3HT chains. Under similar SVA conditions (V_g/V_b ratio of 22/78), only relatively small POMeOPT aggregates with ∼4 ± 1 chains (hereafter denoted as 4-chain POMeOPT aggregate for simplicity) were assembled from single chains. The smaller size of POMeOPT aggregates, relative to *rr*-P3HT, could be ascribed to relatively less favorable packing interactions between POMeOPT chains, as a result of the bulky side chains and the more distorted backbone anticipated with bulkier side chains. These small POMeOPT aggregates have a very similar extent of structural ordering as single chains with mean M value around 0.61 (Figure S8B in the Supporting Information). Different from both cases of *rr*- and *rra*-P3HT, the emission intensity of POMeOPT aggregates is about two times higher than expected based on the number of chains in the aggregates. The slightly increased fluorescence quantum yield of POMeOPT aggregates is somewhat unusual. The stacking distance between the chains likely attenuates the strong interchain electronic coupling that leads to the nonradiative pathways aforementioned in the case of *rr*-P3HT aggregates. But the elimination of the interchain coupling should yield a behavior similar to that of the *rra*-P3HT where the brightness of the aggregates is proportional to the number of chains. Here an additional effect that leads the chains in the aggregates to having a higher quantum yield was observed, potentially due to strong coupling along single polymer chains (intrachain), as will be discussed later on the basis of spectral characteristics of the aggregates.

Next, the effect of pi−pi stacking distance on the interchain energy migration was further examined by comparing the fluorescence blinking behavior of the SVA assembled aggregates of POMeOPT with that of P3HT. Interestingly, the 4-chain POMeOPT aggregates exhibit approximately 4-step fluorescence fluctuation behavior, with each step having similar intensity change, as represented in Figure 3A. This can also be manifested from an average QD of ∼23% in the QD statistical

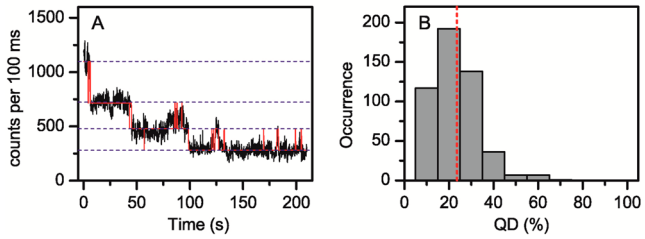

Figure 3. (A) Representative fluorescence transient of a 4-chain POMeOPT aggregate (made from 19 kDa single chains) with the denoised signal overlaid in red (the dashed lines denote counts corresponding to identified emission state). The background signal in the transients is ∼20 counts/100 ms. More fluorescence transients can be found in Figure S9A−C in the Supporting Information. (B) Quenching depth distribution histogram of 4-chain aggregates made from 19 kDa POMeOPT single chains. The red dashed line represents the mean quenching depth.

distribution histogram (Figure 3B) obtained for these 4-chain POMeOPT aggregates. In addition, as the aggregates size increased up to ∼12 ± 3 chains (prepared with a vapor ratio of V_g/V_b of 32/68 (volume ratio of 50/50) in SVA), approximately 10 steps of gradual photobleaching has been identified in the fluorescence transients after denoising (Figure S10 in the Supporting Information). The close proximity of the number of steps observed in the photobleaching to the number of chains in both small and large POMeOPT aggregates suggests that each step of fluorescence fluctuation in the aggregates approximately corresponds to the photobleaching or photorecovery of an individual chain. The chain-by-chain photophysical behavior unravels two important findings: (i) energy migration between individual POMeOPT chains is effectively inhibited; and (ii) intrachain exciton can efficiently migrate along individual POMeOPT chains in the aggregates, presumably due to efficient intrachain electronic coupling between chromophores along the polymer chain. This is in contrast to the observation for the 6-chain *rra*-P3HT aggregates for which there is no obvious chain-by-chain photophysical behavior, inferring a limited exciton migration along *rra*-P3HT chains. This phenomenon is ascribed to disordered single chain conformation of *rra*-P3HT, resulting from disordered aggregation characteristics in the aggregates and/or low regioregularity.

To quantitatively understand how the interchain packing distance affects the interchain energy migration, we examined the distance dependence of the excitonic coupling. Based on the simulation results by Gierschner et al. obtained using an atomistic quantum-chemical approach,[26] it can be estimated that the interchain coupling energy would only drop ∼3 times when the interchain stacking distance increases from 3.8 Å (for P3HT) to 7 Å (for POMeOPT as estimated in ref 27). This implies that the interchain excitonic energy migration rate, which goes as the square of the coupling energy, only decreases by a factor of ∼10. Such a small decrease in the interchain energy migration rate would not be sufficient to make it comparable to or smaller than the intrachain process, considering that the interchain migration rate is typically 2 orders of magnitude higher than the intrachain counterpart.[14,28] Therefore, the packing distance of 7 Å appears insufficient to completely shut off the interchain coupling. Some questions then arise: what are the structures of the POMeOPT aggregates and single chains, how do the bulky side chains keep the backbones apart, and what is a plausible interchain stacking distance range? The above concerns are reasonable especially

dx.doi.org/10.1021/ja508112k | J. Am. Chem. Soc. 2014, 136, 16023−16031

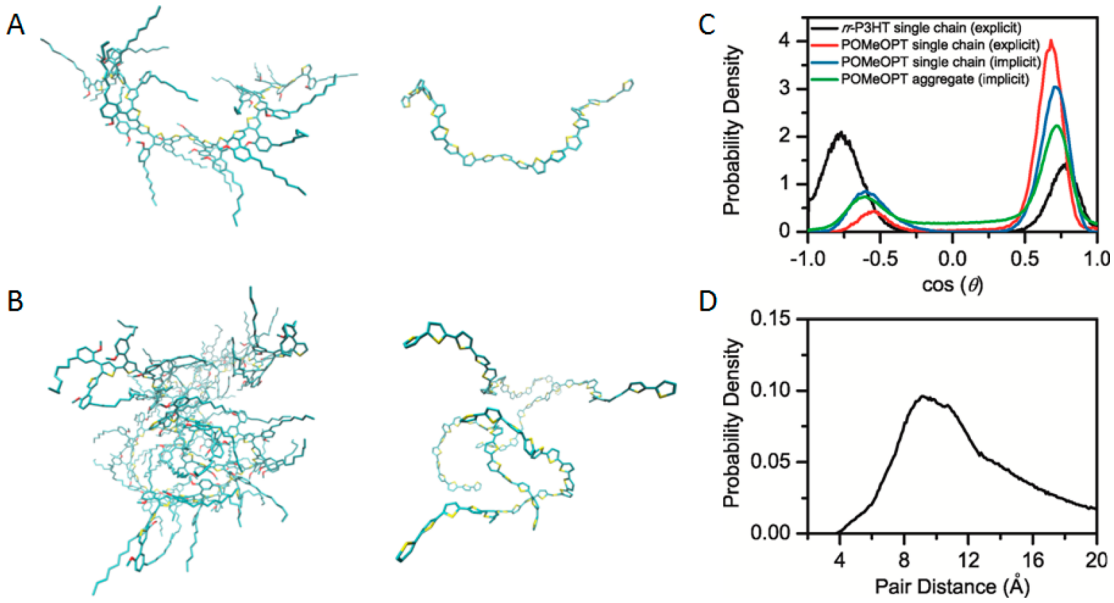

Figure 4. Representative structures of (A) deprotonated POMeOPT single chain with and without side chain taken from the explicit solvent trajectory and (B) deprotonated 4-chain POMeOPT aggregate with and without side chains taken from the implicit solvent trajectory. (C) Backbone dihedral probability distribution for 20-mers of P3HT in toluene (explicit solvent), POMeOPT in toluene (explicit solvent), and both a 20-mer of POMeOPT (implict solvent) and a 4-chain POMeOPT aggregate (implicit solvent) calculated with the scaled potential implicit solvent method described in the Supporting Information. P3HT data is from ref 13b. (D) Probability distribution of minimum thiophene−thiophene ring pair distances for aggregates of POMeOPT. Distances are calculated only over thiophene pairs which are on separate chains.

considering that the referenced packing distance of ∼7 Å was not directly obtained from an X-ray diffraction but calculated from the material density because POMeOPT is less semicrystalline and the diffraction peak from interchain packing is buried in amorphous background.[27]

To offer insight into the structures of POMeOPT aggregates and single POMeOPT chains and provide a plausible packing mechanism and distance, molecular dynamics (MD) simulations were performed. Simulations included a single chain of POMeOPT in explicit solvent toluene, and implicit solvent calculations for a 4-chain aggregate of POMeOPT. All chains were 20 monomer units in length. All MD simulations were calculated with Gromacs v4.6[29] using the OPLS-AA force field,[30] with the SB-T (bond stretch/angle bend/torsion) correction of Dubay et al.[31] Details of the MD simulations can be found in the Supporting Information including a description of the implicit solvent model used for aggregates. Representative structures of a single chain and a 4-chain aggregate of POMeOPT are shown in Figures 4A and 4B, respectively. Of interest is the conformation of the backbone in single chains and aggregates as well as the packing distance in aggregates. Backbone order/disorder is estimated by dihedral angle θ between neighboring thiophene rings as defined and calculated based on our previous approach.[13b] As demonstrated in Figure 4C for the dihedral probability distributions, relative to an equivalent single chain of *rr*-P3HT,[13b] the POMeOPT single chains exhibit a noticeably less planar backbone reflected by the smaller $|\cos(\theta)|$ values, due to the presence of the bulky side chains. This result is in agreement with the low fluorescence excitation anisotropy of POMeOPT single chains (Figure S8A,B in the Supporting Information). Additionally, while *rr*-P3HT slightly favors *trans* for sequential (nearest neighbor) side chains, there is a strong preference for side chains in POMeOPT to adopt a *cis* relationship over *trans*. This leads to quasi-helical sections of the POMeOPT chain, which is anticipated to result in an inhibition of backbone stacking in aggregates. The dihedral distribution of the 4-chain POMeOPT aggregate is approximately consistent with that of the single chain with one subtlety. There is a small baseline isotropic contribution across the range of −0.5 to +0.5 of $\cos(\theta)$ in the dihedral distribution for the POMeOPT aggregate. This baseline isotropy, implying relatively nonplanar dihedrals, is not seen in the single chain distribution, calculated using the same implicit solvent method as the aggregate. This indicates that the baseline isotropy is attributable to the way in which the polymer chains aggregate.

The plausible distance range between thiophene backbones in the simulated POMeOPT aggregates is next examined by considering the distance of thiophene−thiophene pairs on separate chains. As shown in Figure 4D, the minimum pair distance distribution for POMeOPT aggregates is broad and peaked at ∼10 Å. This value is slightly larger than the packing distance of 7 Å estimated previously in bulk films.[27] The variety of aggregate structures sampled includes some separated single chains; the longer distance tail in the distribution is a result of such chains. The longer backbone stacking distance in POMeOPT relative to P3HT is due to the bulky side chains which restrict thiophene−thiophene interaction between neighboring chains. Again using the estimation from Gierschner,[26] it can be estimated that an interchain packing distance of ∼20 Å is required for the interchain energy migration rate to decrease by a factor of ∼100, so that the intrachain migration rate is comparable to the interchain one. Thus, the increased packing distance accounts for a part but not all of the dramatic decrease in interchain energy migration. Compared to the highly ordered *rr*-P3HT aggregates having a mean M of 0.80, the POMeOPT aggregates exhibit slight orientational disorder with a mean M value of 0.61. This relatively disordered interchain packing in POMeOPT

dx.doi.org/10.1021/ja508112k | J. Am. Chem. Soc. 2014, 136, 16023−16031

aggregates plays an additional role in decreasing interchain energy migration, but this contribution seems insignificant.

Although quantum-chemical calculations suggest that the interchain coupling decreases as the chromophore conjugation length becomes infinitely long,[26] the intrachain coupling and its dependence on polymer chain conformation have not been quantified relative to an interchain mechanism. By taking into account exciton motion both along and between polymer chains, the interplay between interchain and intrachain interactions in conjugated polymers has been recently explored by Spano et al. in a so-called HJ-aggregate model.[7c,32] In this model, short-range intrachain order and strong interchain interaction lead to dominant interchain coupling (resembling H-aggregate behavior). In contrast, long-range intrachain order and weak interchain interaction result in strong intrachain coupling (resembling J-aggregate behavior).[7c,32] The chain-by-chain photoblinking behavior in the 4-chain POMeOPT aggregates (19 kDa) demonstrates that, here, there is relatively efficient intrachain coupling along single polymer chains in the aggregates. To experimentally check if there exists such an interplay between the intrachain and interchain couplings, it is informative to interrogate if the interchain energy migration takes place in POMeOPT aggregates composed of shorter single chains in which the intrachain coupling is limited by the size of single polymer chains. We therefore assembled ~5 ± 1 chain POMeOPT aggregates using shorter single chains with M_n of 3.8 kDa (Đ = 1.11). At this molecular weight, the degree of polymerization is ~13, which is equivalent to 1 or 2 chromophores per single chain.[17] The small molecular weight chains and aggregates have similar M distributions (Figure S8C,D in the Supporting Information) as the 19 kDa cases (Figure S8A,B in the Supporting Information). Interestingly, for these small M_n aggregates, chain-by-chain photobleaching behavior is seen in ~80% of the aggregates, but we also observed significant blinking events (with QD > 50%) in ~20% of the aggregates (Figure 5A). The appearance of such large

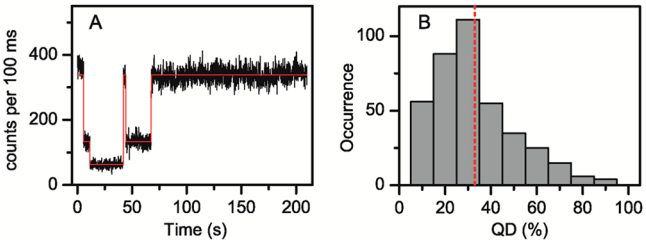

Figure 5. (A) Fluorescence transient of a 5-chain POMeOPT aggregate (made from 3.8 kDa single chains) that exhibits drastic blinking behavior (with the denoised signal overlaid in red line). The background signal in the transients is ~20 counts/100 ms. More fluorescence transients can be found in Figure S9D–F in the Supporting Information. (B) Quenching depth distribution histogram of 5-chain aggregates composed of 3.8 kDa POMeOPT single chains. The red dashed line represents the mean quenching depth.

QD values (Figure 5B) suggests that efficient interchain energy migration occurs within some POMeOPT aggregates composed of short single chains. In the small M_n aggregates, either the intrachain coupling is sometimes (~20%) effectively weakened by the small M_n of single chains and/or the interchain packing is sometimes (~20%) quite favorable, leading to a relative strength of the interchain coupling over the intrachain counterpart. This result reinforces the idea that the photophysics in CPs is strongly dependent on the relative strength of the intrachain and interchain coupling. To understand the nature of the intrachain and interchain couplings, fluorescence spectra were then collected for the single chains and aggregates studied above. As shown in Figure 6, for 19 kDa POMeOPT, compared to the single chains, the

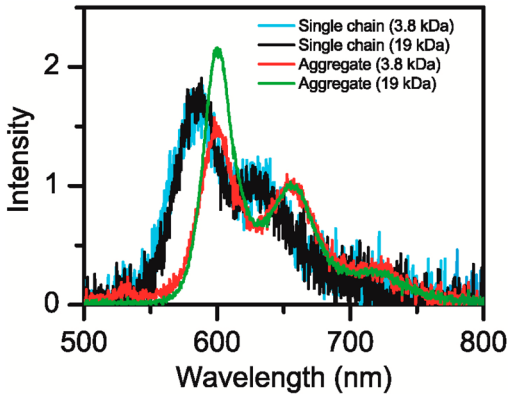

Figure 6. Ensemble fluorescence spectra for single molecules of POMeOPT with M_n of 19 kDa (black) and 3.8 kDa (light blue). Ensemble spectrum for 4-chain POMeOPT aggregates of 19 kDa single chains is shown as green line, and the spectrum for 5-chain aggregates of 3.8 kDa single chains showing QD above 50% is shown as red line. All spectra were normalized at their 0–1 emission maxima for comparison.

aggregates display a pronouncedly enhanced 0–0 emission, characteristic of dominant intrachain coupling (J-aggregate like behavior). In contrast, for the 3.8 kDa POMeOPT aggregates showing pronounced blinking (QD > 50%), the aggregate spectra exhibit a depressed 0–0 emission relative to the spectra of single chains, characteristic of H-aggregate like emission. These results demonstrate that, by reducing the size of polymer chains (i.e., intrachain coupling), the small chains, in fact, more frequently pack into aggregates with interchain H-aggregate type behavior. It can be concluded that the inhibited interchain energy migration observed in the 4-chain POMeOPT aggregates composed of 19 kDa single chains can be attributed to multiple sources working cooperatively: (i) the relatively long interchain separation attenuates the interchain coupling strength; (ii) the relatively disordered packing between POMeOPT chains weakens the interchain coupling; and (iii) there is a persistent intrachain coupling along individual chains in all cases.

■ CONCLUSIONS

To provide a fundamental understanding of the impact of interchain packing morphology on interchain exciton migration in conjugated polymers, modified interchain packing was achieved in solvent vapor annealing constructed polythiophene aggregates by varying the regioregularity and the size of side chains. Photoblinking behavior examined via single aggregate spectroscopy was used as a signature of energy migration in these unique polymer systems. We found that highly ordered interchain packing in *rr*-P3HT is in favor of long-range interchain energy migration, while disordered packing in *rra*-P3HT, even within just a few chains, can significantly impede the interchain mechanism. In contrast to *rr*-P3HT, interchain energy migration is completely inhibited in POMeOPT except for relatively short chain aggregates. The increased interchain packing distance and the relatively disordered packing in

dx.doi.org/10.1021/ja508112k | J. Am. Chem. Soc. 2014, 136, 16023–16031

POMeOPT, obtained from simulated structures, account for a part but definitely not all of the reduction in the interchain excitonic coupling. The competition between intrachain and interchain energy migration mechanisms has been revealed by comparing the POMeOPT aggregates with different polymer chain size. The influence of interchain morphologies on the interchain excitonic energy migration has implications for the morphological dependence of the exciton dynamics occurring after photoexcitation, including the degree of exciton delocalization and relaxation pathways. Our study also highlights the potential for a structural strategy to control energy migration mechanisms by tuning side chain properties such as regioregularity and size.

■ ASSOCIATED CONTENT

Supporting Information

Data on fluorescence transients, modulation distribution histograms, quenching depth histograms, the determination of the number of chains in aggregates, the estimation of energy migration length in *rr*-P3HT, the denoising method of fluorescence transients, the quenching depth analysis, and the molecular dynamics simulations of POMeOPT. This material is available free of charge via the Internet at http://pubs.acs.org.

■ AUTHOR INFORMATION

Corresponding Author

dvandenbout@cm.utexas.edu

Notes

The authors declare no competing financial interest.

■ ACKNOWLEDGMENTS

This material is based upon work supported as part of the program "Understanding Charge Separation and Transfer at Interfaces in Energy Materials (EFRC:CST)", an Energy Frontier Research Center funded by the U.S. Department of Energy (DOE), Office of Science, Office of Basic Energy Sciences (BES), under Award Number DE-SC0001091. P.J.R. acknowledges partial support from the Robert A. Welch Foundation (Grant F-0019). C.F.L thanks the National Science Foundation (Grant CHE-1151647) and the Welch Foundation (Grant C-1787) for support of this work. The fluorimeter was funded by the National Science Foundation (Grant CHE-094750).

■ REFERENCES

(1) (a) Guo, X.; Baumgarten, M.; Muellen, K. *Prog. Polym. Sci.* **2013**, *38*, 1832. (b) Nielsen, C. B.; McCulloch, I. *Prog. Polym. Sci.* **2013**, *38*, 2053. (c) Perepichka, I. F.; Perepichka, D. F.; Meng, H.; Wudl, F. *Adv. Mater.* **2005**, *17*, 2281.

(2) (a) Cornil, J.; dos Santos, D. A.; Crispin, X.; Silbey, R.; Bredas, J. L. *J. Am. Chem. Soc.* **1998**, *120*, 1289. (b) Hwang, I.; Scholes, G. D. *Chem. Mater.* **2011**, *23*, 610. (c) Chang, M. H.; Frampton, M. J.; Anderson, H. L.; Herz, L. M. *Phys. Rev. Lett.* **2007**, *98*, 027402. (d) Spano, F. C.; Silva, C. *Annu. Rev. Phys. Chem.* **2014**, *65*, 477.

(3) (a) Schwartz, B. J. *Annu. Rev. Phys. Chem.* **2003**, *54*, 141. (b) Nguyen, T. Q.; Wu, J. J.; Doan, V.; Schwartz, B. J.; Tolbert, S. H. *Science* **2000**, *288*, 652. (c) Clarke, T. M.; Durrant, J. R. *Chem. Rev.* **2010**, *110*, 6736. (d) Shekhar, S.; Aharon, E.; Tian, N.; Galbrecht, F.; Scherf, U.; Holder, E.; Frey, G. L. *ChemPhysChem* **2009**, *10*, 576.

(4) Bredas, J. L.; Beljonne, D.; Coropceanu, V.; Cornil, J. *Chem. Rev.* **2004**, *104*, 4971.

(5) Hennebicq, E.; Pourtois, G.; Scholes, G. D.; Herz, L. M.; Russell, D. M.; Silva, C.; Setayesh, S.; Grimsdale, A. C.; Mullen, K.; Bredas, J. L.; Beljonne, D. *J. Am. Chem. Soc.* **2005**, *127*, 4744.

(6) (a) Jiang, X. M.; Osterbacka, R.; Korovyanko, O.; An, C. P.; Horovitz, B.; Janssen, R. A. J.; Vardeny, Z. V. *Adv. Funct. Mater.* **2002**, *12*, 587. (b) Guo, J.; Ohkita, H.; Benten, H.; Ito, S. *J. Am. Chem. Soc.* **2009**, *131*, 16869.

(7) (a) Niles, E. T.; Roehling, J. D.; Yamagata, H.; Wise, A. J.; Spano, F. C.; Moule, A. J.; Grey, J. K. *J. Phys. Chem. Lett.* **2012**, *3*, 259. (b) Roehling, J. D.; Arslan, I.; Moule, A. J. *J. Mater. Chem.* **2012**, *22*, 2498. (c) Yamagata, H.; Spano, F. C. *J. Chem. Phys.* **2012**, *136*, 184901. (d) Baghgar, M.; Labastide, J. A.; Bokel, F.; Hayward, R. C.; Barnes, M. D. *J. Phys. Chem. C* **2014**, *118*, 2229.

(8) (a) Bolinger, J. C.; Traub, M. C.; Brazard, J.; Adachi, T.; Barbara, P. F.; Vanden Bout, D. A. *Acc. Chem. Res.* **2012**, *45*, 1992. (b) Lupton, J. M. *Adv. Mater.* **2010**, *22*, 1689. (c) Vacha, M.; Habuchi, S. *NPG Asia Mater.* **2010**, *2*, 134.

(9) (a) Steiner, F.; Vogelsang, J.; Lupton, J. M. *Phys. Rev. Lett.* **2014**, *112*, 137402. (b) Lin, H.; Tabaei, S. R.; Thomsson, D.; Mirzov, O.; Larsson, P.-O.; Scheblykin, I. G. *J. Am. Chem. Soc.* **2008**, *130*, 7042.

(10) (a) Hu, D. H.; Yu, J.; Wong, K.; Bagchi, B.; Rossky, P. J.; Barbara, P. F. *Nature* **2000**, *405*, 1030. (b) Adachi, T.; Brazard, J.; Chokshi, P.; Bolinger, J. C.; Ganesan, V.; Barbara, P. F. *J. Phys. Chem. C* **2010**, *114*, 20896.

(11) (a) Vanden Bout, D. A.; Yip, W. T.; Hu, D. H.; Fu, D. K.; Swager, T. M.; Barbara, P. F. *Science* **1997**, *277*, 1074. (b) Vogelsang, J.; Adachi, T.; Brazard, J.; Bout, D. A. V.; Barbara, P. F. *Nat. Mater.* **2011**, *10*, 942. (c) Park, S. J.; Gesquiere, A. J.; Yu, J.; Barbara, P. F. *J. Am. Chem. Soc.* **2004**, *126*, 4116. (d) Yu, J.; Hu, D. H.; Barbara, P. F. *Science* **2000**, *289*, 1327.

(12) Adachi, T.; Lakhwani, G.; Traub, M. C.; Ono, R. J.; Bielawski, C. W.; Barbara, P. F.; Vanden Bout, D. A. *J. Phys. Chem. B* **2012**, *116*, 9866.

(13) (a) Adachi, T.; Brazard, J.; Ono, R. J.; Hanson, B.; Traub, M. C.; Wu, Z. Q.; Li, Z. C.; Bolinger, J. C.; Ganesan, V.; Bielawski, C. W.; Bout, D. A. V.; Barbara, P. F. *J. Phys. Chem. Lett.* **2011**, *2*, 1400. (b) Hu, Z.; Adachi, T.; Lee, Y.-G.; Haws, R. T.; Hanson, B.; Ono, R. J.; Bielawski, C. W.; Ganesan, V.; Rossky, P. J.; Vanden Bout, D. A. *ChemPhysChem* **2013**, *14*, 4143.

(14) Beljonne, D.; Pourtois, G.; Silva, C.; Hennebicq, E.; Herz, L. M.; Friend, R. H.; Scholes, G. D.; Setayesh, S.; Mullen, K.; Bredas, J. L. *Proc. Natl. Acad. Sci. U.S.A.* **2002**, *99*, 10982.

(15) Andersson, M. R.; Mammo, W.; Olinga, T.; Svensson, M.; Theander, M.; Inganas, O. *Synth. Met.* **1999**, *101*, 11.

(16) Liu, J.; Mikhailov, I. A.; Zou, J.; Osaka, I.; Masunov, A. E.; McCullough, R. D.; Zhai, L. *Polymer* **2011**, *52*, 2302.

(17) Theander, M.; Svensson, M.; Ruseckas, A.; Zigmantas, D.; Sundstrom, V.; Andersson, M. R.; Inganas, O. *Chem. Phys. Lett.* **2001**, *337*, 277.

(18) Brazard, J.; Ono, R. J.; Bielawski, C. W.; Barbara, P. F.; Vanden Bout, D. A. *J. Phys. Chem. B* **2013**, *117*, 4170.

(19) Spano, F. C. *Acc. Chem. Res.* **2010**, *43*, 429.

(20) Kim, Y.; Cook, S.; Tuladhar, S. M.; Choulis, S. A.; Nelson, J.; Durrant, J. R.; Bradley, D. D. C.; Giles, M.; McCulloch, I.; Ha, C.-S.; Ree, M. *Nat. Mater.* **2006**, *5*, 197.

(21) Vohra, V.; Higashimine, K.; Murakami, T.; Murata, H. *Appl. Phys. Lett.* **2012**, *101*, 173301.

(22) Adachi, T.; Brazard, J.; Chokshi, P.; Bolinger, J. C.; Ganesan, V.; Barbara, P. F. *J. Phys. Chem. C* **2010**, *114*, 20896.

(23) Shuang, B.; Cooper, D.; Taylor, J. N.; Kisley, L.; Chen, J.; Wang, W.; Li, C. B.; Komatsuzaki, T.; Landes, C. F. *J. Phys. Chem. Lett.* **2014**, *5*, 3157.

(24) Keum, J. K.; Xiao, K.; Ivanov, I. N.; Hong, K. L.; Browning, J. F.; Smith, G. S.; Shao, M.; Littrell, K. C.; Rondinone, A. J.; Payzant, E. A.; Chen, J. H.; Hensley, D. K. *CrystEngComm* **2013**, *15*, 1114.

(25) Lim, J. A.; Liu, F.; Ferdous, S.; Muthukumar, M.; Briseno, A. L. *Mater. Today* **2010**, *13*, 14.

(26) Gierschner, J.; Huang, Y.-S.; Van Averbeke, B.; Cornil, J.; Friend, R. H.; Beljonne, D. *J. Chem. Phys.* **2009**, *130*, 044105.

(27) Aasmundtveit, K. E.; Samuelsen, E. J.; Mammo, W.; Svensson, M.; Andersson, M. R.; Pettersson, L. A. A.; Inganas, O. *Macromolecules* **2000**, *33*, 5481.

(28) Wong, K. F.; Bagchi, B.; Rossky, P. J. *J. Phys. Chem. A* **2004**, *108*, 5752.
(29) Hess, B.; Kutzner, C.; van der Spoel, D.; Lindahl, E. *J. Chem. Theory Comput.* **2008**, *4*, 435.
(30) Kaminski, G. A.; Friesner, R. A.; Tirado-Rives, J.; Jorgensen, W. L. *J. Phys. Chem. B* **2001**, *105*, 6474.
(31) DuBay, K. H.; Hall, M. L.; Hughes, T. F.; Wu, C. J.; Reichman, D. R.; Friesner, R. A. *J. Chem. Theory Comput.* **2012**, *8*, 4556.
(32) Yamagata, H.; Hestand, N. J.; Spano, F. C.; Kohler, A.; Scharsich, C.; Hoffmann, S. T.; Bassler, H. *J. Chem. Phys.* **2013**, *139*, 114903.